

Numerical Analysis of Wind Turbines Blade in Deep Dynamic Stall

Hamid Reza Karbasian^a, Javad Abolfazli Esfahani^{b,c,e,*}, Aliyu Musa Aliyu^d, Kyung Chun Kim^{e,*}

^a*Department of Mechanical, Industrial and Aerospace Engineering, Concordia University, Montreal, Canada.*

^b*Mechanical Engineering Department, Ferdowsi University of Mashhad, Mashhad, Iran.*

^c*Center of Excellence on Modelling and Control Systems, (CEMCS), Ferdowsi University of Mashhad, Iran.*

^d*School of Computer and Engineering, University of Huddersfield, Queensgate, HD1 3DH, UK.*

^e*School of Mechanical Engineering, Pusan National University, Busan 609-735, Republic of Korea.*

Abstract

This study numerically investigates kinematics of dynamic stall, which is a crucial matter in wind turbines. Distinct movements of the blade with the same angle of attack (AOA) profile may provoke the flow field due to their kinematic characteristics. This induction can significantly change aerodynamic loads and dynamic stall process in wind turbines. The simulation involves a 3D NACA 0012 airfoil with two distinct pure-heaving and pure-pitching motions. The flow field over this 3D airfoil was simulated using Delayed Detached Eddy Simulations (DDES). The airfoil begins to oscillate at a Reynolds number of $Re = 1.35 \times 10^5$. The given attack angle profile remains unchanged for all cases. It is shown that the flow structures differ notably between pure-heaving and pure-pitching motions, such that the pure-pitching motions induce higher drag force on the airfoil than the pure-heaving motion. Remarkably, heaving motion causes excessive turbulence in the boundary layer, and then the coherent structures seem to be more stable. Hence, pure-heaving motion contains more energetic core vortices, yielding higher lift at post-stall. In contrast to conventional studies on the dynamic stall of wind turbines, current results show that airfoils' kinematics significantly affect the load predictions during the dynamic stall phenomenon.

Keywords: Wind energy, Wind turbine, Dynamic stall, Fluid-Structure Interaction (FSI), Computational Fluid Dynamics (CFD), Renewable energy.

1. Introduction

Dynamic stall is a common phenomenon in aerodynamics, which involves a series of flow separations accompanied by reattachments on the surface of the airfoil due to rapid changes in the angle of attack. These changes could be due to rapid unsteady movement of blades, such as rotational and translational motions. Deep dynamic stall is referred to as process of the formation and shedding of the Leading Edge Vortex (LEV) on the suction side of the airfoil, where complex flow structures are created due to highly non-linear flow regime in wake. In the helicopter rotors' design, dynamic stall is considered in a small range of angles of attack to prevent the helicopter rotors from experiencing a deep dynamic stall [1, 2, 3]. However, a deep dynamic stall occurs in wind turbines [4, 5, 6, 7, 8, 9]. One of the essential factors in wind turbines is the aerodynamic loads'

*Corresponding author

Email addresses: Abolfazli@um.ac.ir (Javad Abolfazli Esfahani), kckim@pusan.ac.kr (Kyung Chun Kim)

accuracy for each blade section. These aerodynamic loads undergo massive changes when a blade is subjected to dynamic stall. Large hysteresis can occur when a deep dynamic stall appears.

The dynamic stall occurs typically at high angles of attack (AOA) than the static stall, so the blade's aerodynamic behaviour would be quite different [3, 10, 11, 12]. Any unsteadiness in the flow velocity or direction causes the advent of the dynamic stall in wind turbines [10]. Unsteadiness could occur from yawed wind, gusts, or large-scale atmospheric turbulence. Another essential part is the kinematics of the wind turbine blades during unstable conditions. The requisite kinematic behaviours that lead to deep dynamic stall are the bending fluctuation of flexible blades, changes in the blades' pitch angle, and the yawing of the turbine [13, 14, 15, 16].

Dynamic stall is a primary phenomenon in Vertical Axis Wind Turbines (VAWTs) since the angle of attack of the blades is continuously changing [17, 18, 19]. These changes in the angle of attack are due to the rotational motion of the blade, represented by a pitching motion. However, these turbines do not experience any translational motion. On the other hand, Horizontal Axis Wind Turbines (HAWTs) can have both rotational and translational motions [14, 20, 21]. This translational motion often occurs due to the oscillation of flexible blades during the rotation of blades around the horizontal axis. Therefore, in this study, we focus on HAWTs since they often have both kinematics. However, it can be attributed to VAWTs if we consider adding any translational motion in the blades due to any vibration or deflection. To investigate dynamic stall, a pure-pitching motion is applied to an airfoil, and the AOA is changed frequently with respect to the free-stream velocity. Karbasian and Kim [22] considered a purely pitching airfoil and found that there is a pairing between counter-rotating core vortices from the leading and trailing edges of the airfoil in deep dynamic stall. Gharali and Johnson [13] considered deep dynamic stall for a stationary airfoil by continuous changes in the direction of free-stream flow. Their objective was to study the effect of unsteady wind directions on the dynamic stall of the airfoil in wind turbines. They found that unsteadiness in the free-stream may cause some severe variations in the aerodynamic loads due to strong changes in the strength of core vortices in dynamic stall. Other extensive studies have also examined the dynamic stall of a pitching airfoil [2, 22, 23, 24], and other applications of the dynamic stall in bio-inspired propulsion and energy extraction can be found in [25, 26, 27, 28, 29].

In heaving motion, there are a wider range of conditions under which a heaving airfoil can produce thrust compared to the pitching motion. At low oscillation frequencies in the heaving motion, Leading-Edge Vortices (LEVs) interaction with Trailing-Edge Vortices (TEVs) produces a new wake structure that resembles a mushroom [23]. However, at higher oscillation frequencies of the airfoil, the interaction of LEVs and TEVs creates a jet-like wake structure known as inverse von-Karman streets [30]. Jones et al. [31] reported that these inverse von-Karman streets occur at relatively high heaving velocities. The heaving amplitude and oscillation frequency have a notable effect on the aerodynamic loads, and flow structures. Young and Lai [32] observed that the generation of aerodynamic loads for pure-heaving airfoil is highly influenced by oscillation frequency. Additionally, as oscillation frequency reduces, the heaving amplitude should be increased to produce thrust. They also showed that thrust generation is possible in higher oscillation frequencies and lower heaving amplitudes [33]. However, Davari [34] showed that wake structure for a heaving airfoil could produce drag, thrust,

or nothing (i.e., neither drag nor thrust), depending on the mean AOA, heaving amplitude, and oscillation frequency. When a heaving airfoil produces thrust, a high-momentum jet flow is created in the center of the wake region, in contrast to conventional low-momentum flow. The momentum loss in the wake region also reduces according to the increasing of the reduced frequency.

Most studies have used pure-pitching motion to study the dynamic stall, especially for wind turbines. There is no comprehensive study on the effects of different kinematics on aerodynamic features. The primary studies have been done based on the AOA profile, Reynolds number, unsteadiness in the free-stream flow, and oscillation frequencies. Above all, there is no comprehensive study on blades' motion to see how aerodynamic loads can be affected by kinematic parameters. In other words, two distinct movements may produce the same AOA profile, but their kinematic characteristics may provoke the flow field. This induction can significantly change aerodynamic loads. Our previous experimental study in [35] addressed this issue for low Reynolds numbers. Particle Image Velocimetry (PIV) measurements were taken into account to figure out the flow structures and load prediction. In this Reynolds number, the flow structures are not very different from each other to distinguish them according to the kinematics. Therefore, this study numerically investigates this issue to uncover the impact of the kinematics on the three-dimensional flow at a high Reynolds number.

Medjroubi et al. [36] established a high-order numerical simulation to study the Reynolds number, mean incidence and sinusoidal heaving motion of a two-dimensional airfoil. In their simulations, two-dimensional Navier–Stokes equations were solved using a spectral element method for the spatial discretization and a high-order splitting scheme for temporal discretization. Hand et al. [37] numerically investigated the dynamic stall for a two-dimensional NACA 0018 airfoil with pitching motion. They used the Unsteady Reynolds-Average Navier–Stokes (URANS) method and Detached Eddy Simulation (DES) method for a 2D domain, and the results were compared. Kim and Xie [10] studied the effects of the free-stream velocity on a pitching airfoil's aerodynamic performance in the deep dynamic stall using Large Eddy Simulations (LES). They found that turbulence in the free-stream velocity significantly affected the lift coefficient during the down-stroke. The inertial sub-range yields the extension of the turbulent flow's pitching mode, but there is a distinctive spectral gap for laminar flow. Almohammadi [18] investigated the dynamic stall of a pitching NACA 0012 airfoil using computational fluid dynamics (CFD). They used a 2D URANS method with a transition SST model for turbulence modelling. The laminar-turbulence transition was a crucial factor in the design and optimization process. Yao et al. [38] investigated the transitional effect on the flow separation and dynamic stall of a pitching airfoil. They observed that the interaction between the three-dimensional stream-wise vortices has a notable effect on the turbulent flow in the dynamic stall phenomenon. Additionally, they observed the LEVs seem more stable at a higher reduced frequency, decreasing the lift fluctuation in the dynamic stall. As mentioned before, there is no any thorough study on the effect of the airfoil kinematics on the dynamic stall and the generation of aerodynamic loads. This study investigates deep dynamic stall for both pure-pitching and pure-heaving motions. This work's motivation is to set the identical boundary conditions and AOA profile for both pure-pitching and heaving motions and observe kinematics' influence on the aerodynamic features (i.e., flow structures and aerodynamic loads). The CFD tool was applied to simulate the flow field around a moving

airfoil. Delayed Detached Eddy Simulations (DDES) approach is used to increase the accuracy of simulations and obtain more realistic flow structures in the wake region. The results are compared to determine kinematics' influence on the flow structure, turbulence, and aerodynamic loads.

2. Physical model

Figure 1 shows the kinematics and parameters of the dynamic stall for a wind turbine. The airfoils can fluctuate due to bending, and it leads to transversal motion along the pitching axis. A flexible airfoil can bend in each direction, but the displacement in y direction (flapwise) is more extensive than in x direction (edgewise). Therefore, we neglect the transversal motions in x direction. The transversal motion in y direction adds an additional velocity component, which leads to changes in the effective AOA along the airfoil. This airfoil may

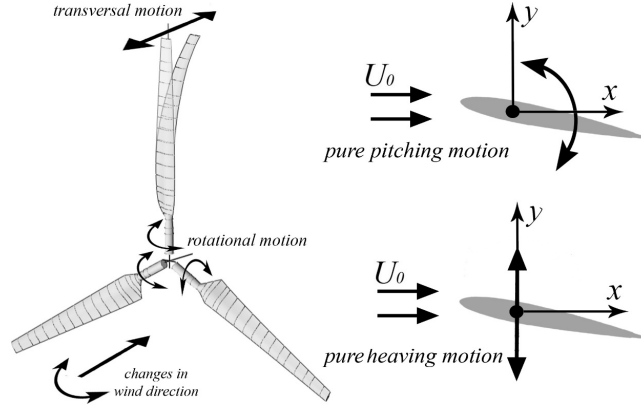


Figure 1: Dominant variations in wind turbine and schematic of airfoil motion for one segment of a airfoil.

have rotational motion around the pitch axis to change aerodynamic loads. This rotational motion leads to pitching motion and can change the effective AOA along the airfoil. Note that there is also twist that may deform a flexible airfoil around the pitch axis, which causes some changes in AOA. However, for simplicity we neglect this deformation and only consider dominant motions for a flaxible airfoil. Changes in wind speed or direction due to background atmospheric turbulence are also responsible for variations in the AOA angle, and it causes the dynamic stall. However, other motions like yawing and even changes in the turbine's rotational speed may cause the dynamic stall, which is not considered in this work. The various motions can be categorized as pure-heaving and pure-pitching motions. One or both of these distinct kinematic motions can cause the dynamic stall. The pure-pitching is an oscillation of the airfoil around a pitching axis. The angle between the chord line and free-stream velocity, U_0 , represents an effective AOA. In the case of pure-heaving motion, the airfoil has reciprocal motion in y direction. This motion in y direction forms additional velocity components. The combination of heaving and free-stream velocities, which are normal and parallel to the chord line, respectively, forms a new effective AOA. The heaving motion is a sinusoidal motion along y direction

$$h(t) = h_m \sin(2\pi ft), \quad (1)$$

106 where h_m , f , and t are the heaving amplitude, oscillating frequency, and time, respectively. Additionally, the lift and drag coefficients are represented by

$$C_L = \frac{L}{0.5\rho c U_0^2}, \quad C_D = \frac{D}{0.5\rho c U_0^2}, \quad (2)$$

108 where L and D are lift and drag forces acting on the airfoil's aerodynamic center. Also, ρ and c are fluid density and chord length, respectively. Note that lift and drag forces are normal and tangent to the total velocity, 110 respectively. Hence, the effective angle of attack is an angle between the chord line and total velocity. Hence, the effective angle of attack α for a airfoil with heaving motion is

$$\alpha(t) = \alpha_0 + \tan^{-1} \left[\frac{2\pi f h_m}{U_0} \cos(2\pi f t) \right], \quad (3)$$

112 where α_0 is the initial angle, which is constant. It is defined as the angle between the free-stream velocity and chord line at $t = 0$. On the other hand, if the agent for the AOA variations is the pitching motion around the 114 quarter-chord, the AOA can be written as follows:

$$\alpha(t) = \alpha_0 + \alpha_m \sin(2\pi f t + \phi), \quad (4)$$

where α_m is the pitching amplitude, and ϕ is the phase angle between two motions, which is set to $\phi = 90^\circ$ for 116 all cases in this study. The oscillating frequency is usually given by a non-dimensional form that is called the reduced frequency:

$$k = \frac{\pi f c}{U_0}, \quad (5)$$

118 where the reduced frequency is the ratio of the convective time scale and the forced oscillation time scale. The Reynolds number is also defined as follows:

$$Re = \frac{\rho c U_0}{\mu}, \quad (6)$$

120 where μ is fluid viscosity. The pure-heaving and pure-pitching have their unique formulation for the effective AOA. If these motions produce an equivalent effective AOA profile, the dynamic stall results may or may not 122 be the same for both cases. The same effective AOA profiles are used as input for both pure-heaving and pure-pitching motions to find out this phenomenon. Then the aerodynamic and flow structures for both cases 124 are considered. Another definition for the aerodynamic load is non-dimensional forces in x and y directions, which is given by

$$C_y = \frac{F_y}{0.5\rho c U_0^2}, \quad C_x = \frac{F_x}{0.5\rho c U_0^2}, \quad (7)$$

126 where, F_y and F_x are forces in y and x directions, with respect to free-stream velocity.

3. Numerical model

128 To numerically investigate the flow field in the deep dynamic stall, a computational fluid dynamics flow solver ANSYS Fluent version 16.1 (ANSYS Fluent, Academic Research, V16.1 2015) is employed. In the case 130 of the 3D flow simulation, the incompressible flow pattern is computed using DDES. The flow field outside of the boundary layer is resolved based on the LES. However, eddies are filtered based on spatial filtering and

resolved. The turbulent flow inside the boundary layer is modelled based on URANS. In this case, the flow inside the boundary layer is modelled using Shear Stress Transport (SST) $k-\omega$ model to predict the turbulence properties. The spatial discretization methods for the momentum and turbulence formulation are the bounded central differencing and second-order upwind methods, respectively. The transient formulation is the second-order implicit method. Additionally, the Pressure Implicit with Splitting of Operator (PISO) method is used in computations to couple the pressure-velocity. Additionally, the time step selected is $\Delta t = 15 \times 10^{-5}T$, where T is oscillating cycle. Note that the results are presented for the seventh oscillating cycle to make sure the flow is completely developed in the computational domain. In this case, the CFL number is lower than 2. The Reynolds number ($Re = 1.35 \times 10^5$) is similar (the same order of magnitude) to the Reynolds number considered for medium and small-sized wind turbines. However, this Reynolds number is approximately one order of magnitude lower than values considered for large scale wind turbines. It is essential to see whether the Reynolds number can be representative of flow at higher angles of attack. Lissaman [39, 40] indicated that $Re \approx 7 \times 10^4$ is a critical value between low and high Reynolds number. Since the Reynolds number in this work is far higher than this criterion, the present study could extend the results and examinations them for the medium and large-scale wind turbines.

3.1. Grid design

Figure 2 displays the three-dimensional computational domain designed with a popular C-mesh topology. The thickness of the domain (the airfoil span) is selected as one chord length. A distance of approximately $20c$ is chosen for the outer boundaries from the airfoil to avoid any boundary reflection. Moreover, this distance was sufficient to eliminate the effect of boundary reflection on the airfoil flow structure, hence the aerodynamic loads. A total of 9.4×10^6 nodes for the final design and 250 nodes are placed along the airfoil and clustered close to the nose and trailing edges.

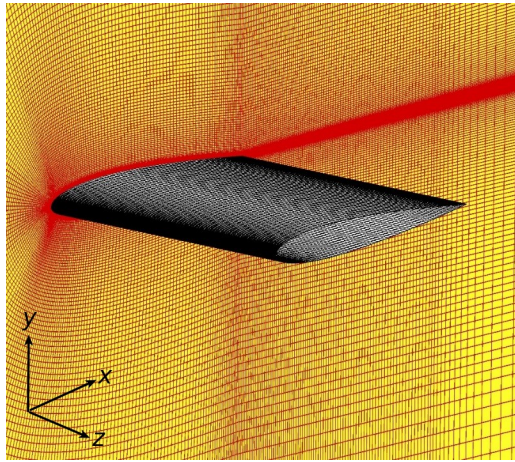


Figure 2: Designed mesh with structured topology for a 3D airfoil.

To design a structured 3D computational domain, first of all, a 2D case with the same boundary conditions is run to compute the boundary layer thickness. Then, based on the boundary layer thickness, the spatial step size was computed for the design of the 3D domain. It is worth pointing out that the boundary layer is a critical

point in the mesh design for DDES computations because the flow is modelled inside of the boundary layer and is solved elsewhere. The boundary layer thickness would be different if the airfoil were in motion. However, when the flow is still attached to the wall, the maximum boundary layer thickness was taken into account for our design purpose.

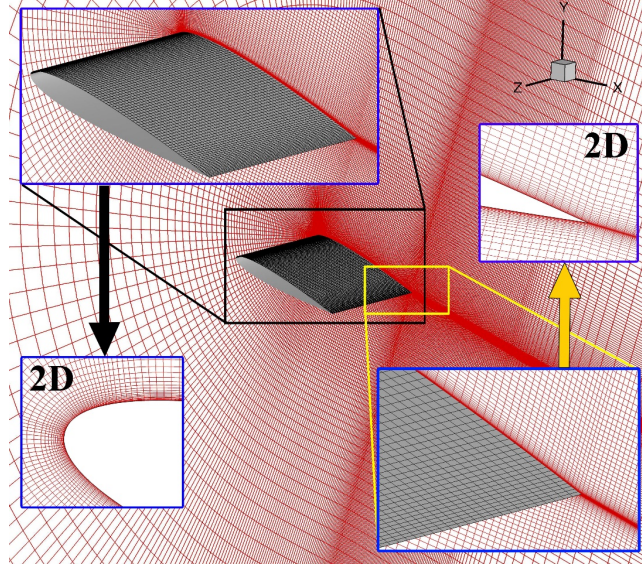


Figure 3: Computational domain and close-up view of detailed mesh topology.

The 2D mesh was extruded through the z direction (span-wise) with a spatial step size of $\Delta z = 0.0125c$. Figure 3 shows more details regarding the computational domain. The mesh has a uniform distribution in the z -direction. The leading and trailing edges are magnified to show the details of the structured mesh in those regions. The airfoil is encompassed by a boundary mesh normal to the wall with y^+ lower than 1. A 2D view also shows the precision of the mesh around the leading and trailing edges. Near the trailing edge, the mesh is kept dense and fine to capture the mixing layer behind the airfoil at low angles of attack. The airfoil is set to no-slip condition, and the side boundaries are periodic. The inlet and outlet of the computational domain are set to a velocity inlet and atmospheric pressure outlet.

3.2. Solution time and grid sensitivities

To verify the computational method, different computational domains are devised and examined with the same boundary conditions. A pitching airfoil with a reduced frequency of $k = 0.05$ and the effective AOA of $\alpha = 10^\circ + 15^\circ \sin(\omega t)$ is selected as a benchmark for the case study. Moreover, four different computational domains are designed according to Table 1. In this table, N_z describes the nodes in the span-wise direction. Additionally, the nodes on the airfoil's surface $N_{air,foil}$, and the total number of nodes in the entire computational domain N_{total} is given. Firstly, a satisfactory resolution was determined for x and y directions with a reasonable number of nodes in the z direction. Then, the N_z value was raised to see whether the number of nodes is adequate in the span-wise direction. The number of nodes in the span-wise direction was $N_z = 1.6 \times 10^2$ in the A1, A2, and A3 cases, but it was increased to $N_z = 2.0 \times 10^2$ for the A4 case. The number of nodes on the airfoil

Type	N_{total}	$N_{airfoil}$	N_z	Mean absolute error (C_L)
A1	52×10^5	2×10^2	1.6×10^2	0.17
A2	76×10^5	2.5×10^2	1.6×10^2	0.030
A3	94×10^5	2.5×10^2	1.6×10^2	0.019
A4	117×10^5	2.5×10^2	2.0×10^2	-

Table 1: Results for different computational domains.

surface is $N_{wall} = 2.0 \times 10^2$ in the coarse grid case (A1) and $N_{wall} = 2.5 \times 10^2$ for the rest. Figure 4 compares the lift coefficient history for one oscillating period. The results provided are for the 7th cycle to make sure transition effects (due to the initial condition) are vanished from domain. However, since the flow is limit cycle (or aperiodic) in this problem, we expect to get the same aerodynamic force for each cycle. A1 (coarse grid) under-predicts the lift coefficient. Domains with coarse grid size have high spatial errors, and in this case, the computations become more dissipative. Therefore, the kinetic energy in the flow and the strength of core vortices decrease significantly. Additionally, the decreasing kinetic energy in the boundary layer advances the separation point, stall, and vortex shedding.

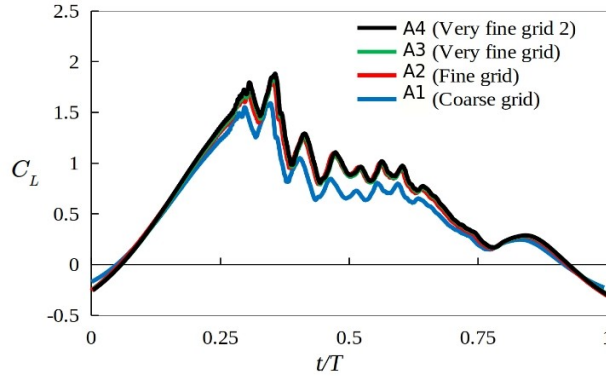


Figure 4: Instantaneous lift coefficients for different grid resolutions: A1 (coarse grid, 52×10^5 nodes), A2 (fine grid, 76×10^5 nodes), A3 (very fine grid, 94×10^5 nodes), A4 (extra fine grid, 117×10^5 nodes).

Case A2 (fine grid) shows an increase of the instantaneous lift coefficient, representing the increase in core vortices' strength. In this case, the computational domain is not as dissipative as in the case A1, and it shows less spatial error in computations. Therefore, eddies have more kinetic energy in turbulent flow and lead to strong core vortices with high circulation in the post-stall region. A3 has a very fine grid, but its difference from A2 is negligible. However, A3 represents slightly higher lift force, which indicates a low round-off error in the computations. Case A4 also shows another fine domain, similar to A3, but it has different mesh layers in the z direction. Increasing N_z has no significant influence on the flow features and lift coefficient, indicating that case A3 has enough number of grids in z direction. Moreover, the mean absolute error for C_L was computed for all cases with reference to case A4, as it is shown in Table 1. The mean absolute error is 17.6% for case A1, but 3.02% and 1.96% for cases A2 and A3, respectively. Therefore, the case A3 is chosen as the appropriate computational domain since its error difference with the case A4 is negligible.

The lift and drag coefficients for a pitching airfoil are considered to validate our numerical results in the 3D domain. The present numerical results for 3D NACA 0012 airfoil are compared with the CFD [10] and experimental [41] results. Kim and Xie [10] used the LES approach to investigate the dynamic stall's turbulence effect. In their simulations, the numbers of mesh nodes around the upper and lower sides of the airfoil are 386 and 193, respectively, with 20 nodes in spanwise direction. In the experimental case, the aerodynamic loads were acquired by surface pressure measurements in different locations over the airfoil. In this case study, the AOA profile is $\alpha = 10^\circ + 15^\circ \sin(\omega t)$, and two reduced frequencies $k = 0.05$ and $k = 0.1$ are considered. In the present study, all aerodynamic loads are computed based on integration over the airfoil's entire surface; Kim and Xie [10] also used the same method.

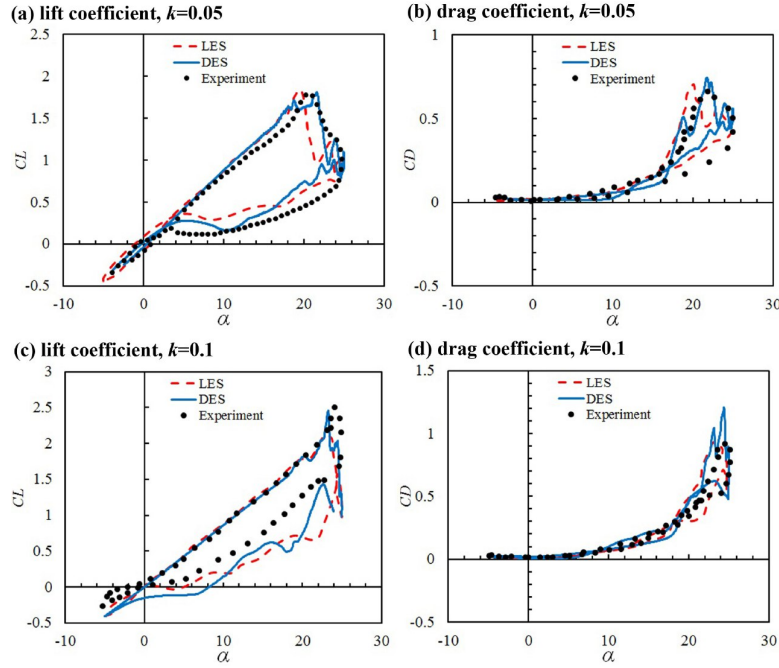


Figure 5: Comparison of DDES results with LES numerical results and experimental data [41]. In this case, the airfoil has pure-pitching motion with $Re = 1.35 \times 10^5$ and reduced frequencies of $k = 0.05$ and $k = 0.1$.

Figure 5 illustrates the comparison of the numerical simulations. Figures 5(a) and 5(b) show hysteresis in the lift and drag coefficients versus the AOA for a pitching airfoil at $k = 0.05$. As shown in Figure 5(a), the DDES results are in close agreement with the LES results in the pre-stall region, where the lift coefficient variation is linear. With increasing the AOA in the up-stroke, some discrepancies are highlighted between the numerical and experimental results. In the wind tunnel's experimental measurements, the surface pressure measurements at high values of the reduced frequencies are difficult because of the deep stall's complex flow structures. Thus, these kinds of discrepancies are expected.

The LES results predict dynamic stall earlier than the experiment, while the DDES results show that dynamic stall occurs slightly later. This discrepancy could be due to the fundamental differences between the LES and DDES approaches. However, the DDES results show a better prediction of the lift coefficient between

the dynamic stall angle and maximum AOA ($\alpha = 25^\circ$). There are always some discrepancies between the numerical and experimental results due to the flow complexity in the down-stroke phase. Furthermore, this discrepancy can also originate from deviations in the first LEV prediction.

In Figure 5(b), the drag coefficient in the DDES results shows better prediction with respect to the experimental data in the up-stroke phase. In contrast, in the down-stroke phase, it over-predicts the drag compared to the LES results, when the AOA is still high ($17^\circ < \alpha < 25^\circ$). As the AOA decreases, the results of DDES match those of LES and experiment. Figures 5(c) and 5(d) illustrate the lift and drag coefficients for a pitching airfoil at a reduced frequency $k = 0.1$. As shown in Figure 5(c), the lift coefficient increases linearly in the pre-stall region by increasing the AOA. The DDES results show good agreement with both the LES and experimental results. DDES correctly predicts the maximum lift coefficient with a small difference in the AOA at the dynamic stall point, while the LES results represent a lower peak lift for this case. In the down-stroke phase, the discrepancies between the experimental and numerical results increase due to post-stall complexity, and DDES results have similar trends to the LES results. In Figure 5(d), the drag coefficient for DDES shows good agreement with both the experimental and LES results. As the AOA increases, DDES results follow LES's trends and the experimental results, but DDES predicts a higher drag coefficient near the stall zone than LES results.

As mentioned, the discrepancies between the numerical and experimental results might be due to the challenging methods used in the experiment. The differences between DDES and LES results could also be due to different basic concepts and theories used in these approaches. Additionally, it might be due to the other numerical procedures chosen for the computations. The mesh quality significantly influences the numerical results, particularly skewness and the number of nodes around the airfoil, which impact numerical results in boundary layer and wake of the airfoil.

4. Results and discussion

4.1. Pressure field and behaviour of vortices

The vortices play an essential role in the instability of dynamic stall. Tracking the pressure field and vorticity magnitude shows how it might influence the oscillating airfoil's aerodynamic performance. In this case, Figure 6 to Figure 9 are provided. Figure 6 shows the vorticity contours in the z direction for pure-heaving. When the AOA is in the range of -5 to 5° , Figures 6 (a), 6(b), and 6(c), the flow is attached to the airfoil surface, and vortices mostly appear as a vortex sheet that is shed into the wake. When the AOA is 10° , Figure 6(d), the flow begins to separate from the trailing edge, and the separation point advances toward the leading edge as the effective AOA increases. As shown in Figure 6(e), when the AOA is 20° , a separation bubble forms and develops into LEV. At this instant, the lift force begins to increase, and von-Karman streets start to shed into the wake. At the AOA 25° , Figure 6(f), the primary LEV pinches off, and TEV has grown adequately to shed. At this moment, the lift coefficient drops due to the TEV formation.

When the AOA decreases, Figure 6(g), the TEV separates from the trailing edge and sheds into the wake. At this instant, secondary LEV is still on the airfoil's suction side, and it covers the surface. In Figure 6(h),

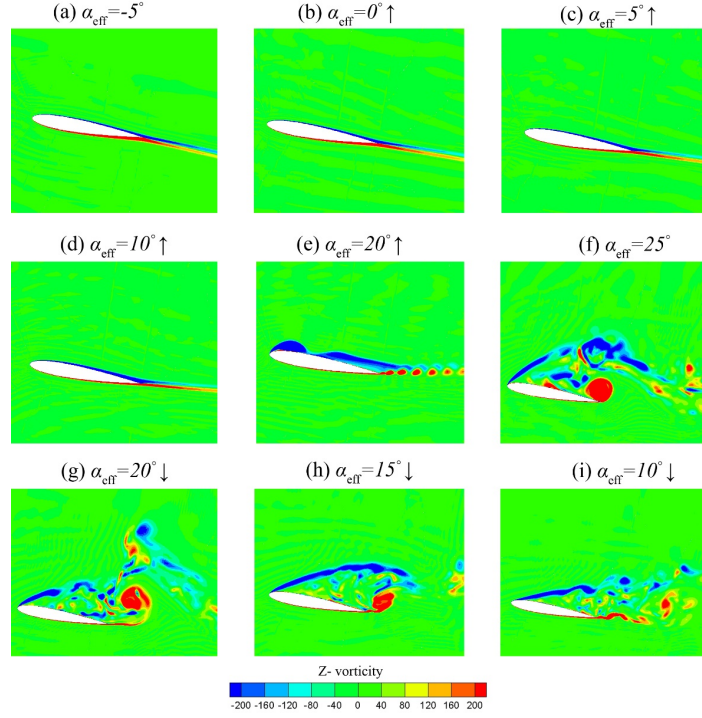


Figure 6: Vorticity contours in the z direction for pure-heaving at $k = 0.1$.

the AOA reaches 15° , and the flow is massively separated. At this moment, the secondary TEV develops and pinches off. With further decreasing of the AOA, the flow is still separated, but it tends to attach to the suction side. Figure 7 illustrates the vorticity contours for pure-pitching motion. When the AOA is in the range of -5 to 5° , Figures 7(a), 7(b), and 7(c), the flow is fully attached to the airfoil surface. The vortex sheet comprises von-Karman streets at a small scale at which the grid size does not allow for precise simulation. Figure 7(e) displays that the separation bubble grows as the AOA increases. In this case, flow is partially separated on the suction side of the airfoil, and von-Karman street shedding occurs. In Figure 7(f), AOA reaches its maximum value, and at this moment, primary LEV and TEV separate from the airfoil, and shed into wake.

As it is shown in Figure 7(g), when the effective AOA decreases the secondary LEV develops, and becomes stronger. This results in another lift peak in the profile during the down-stroke phase [22]. Additionally, TEV separates from the trailing edge and shed into the wake. With a further decrease in the AOA, the flow entirely separates, and the dominant core vortices cannot develop, Figure 7(h). As the angle of attack decreases, shear layer at the leading edge loses its power to produce dominant core vortices. Therefore, it is expected that the wake region does not contain any core vortices until up-stroke phase occurs again. At lower AOAs, Figure 7(i), minor core vortices appear and shed like von-Karman streets. However, the flow tends to detach from the airfoil surface at lower angles of attack.

Figure 8 illustrates the pressure distribution about a pure-heaving airfoil at $k = 0.1$. In Figure 8(a), the AOA is -5° , and a low-pressure zone is created on the lower side of the airfoil. With increasing the AOA to positive values from 0° to 5° , Figures 8(b) and 8(c), a low-pressure zone begins to develop on the upper side of the airfoil. Figure 8(d) shows that the low-pressure zone begins to grow and envelops the airfoil's suction

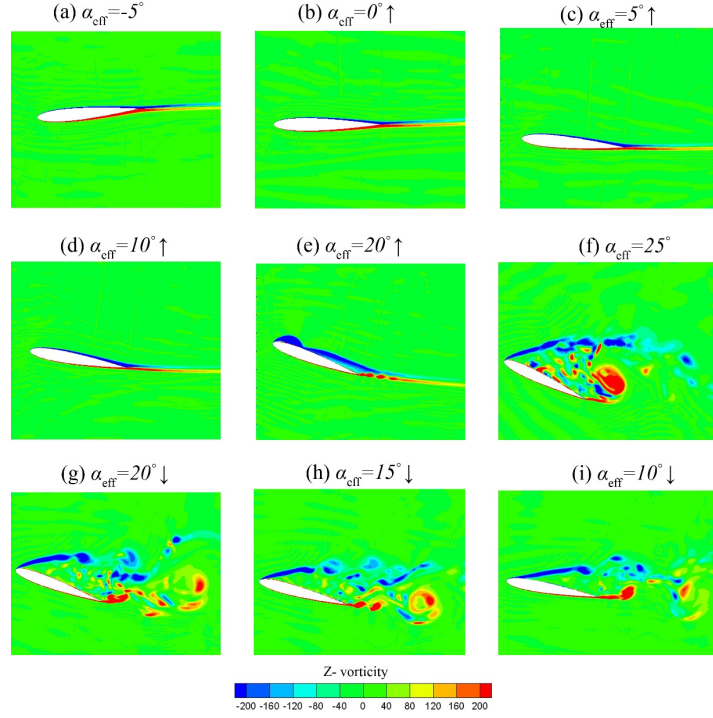


Figure 7: Vorticity contours in the z direction for pure-pitching at $k = 0.1$.

side. At this moment, the shear layer at the leading edge is the main cause of separation bubbles. As the AOA increases, the low-pressure zone on the airfoil's suction side becomes dominant and envelops the entire upper surface. Near the leading edge, the negative pressure has a higher value due to a primary LEV presence.

Figure 8(f) shows post-stall instant when the TEV formed and covered a part of the airfoil's lower side. At this moment, the lift coefficient drops significantly. In Figure 8(g), the low-pressure zone still covers the airfoil's upper side, while highly negative pressure zones indicate core vortices' presence. In Figure 8(h), the low-pressure zone loses its magnitude, and hence, the aerodynamic forces decrease, and von-Karman vortex shedding occurs as the AOA decreases, Figure 8(i). Figure 9 illustrates the pressure coefficient contours around a pure-pitching airfoil at $k = 0.1$. In Figure 9(a), $\alpha_{eff} = -5^\circ$, negative pressure is on the lower surface of the airfoil. When AOA is zero, both sides of the airfoil do not have equivalent pressure contours. This is because the airfoil has a motion, either upstroke or downstroke, which deviates flow in one direction more than the others, as opposed to a stationary airfoil. However, this difference is not significant and has a negligible effect on the aerodynamic loads. With increases in AOA, from 5° to 10° , as shown in Figures 9(c) and 9(d), negative pressure becomes prominent near the leading edge of the airfoil. This low-pressure region is responsible for shear layer formation and, hence, the separation bubble formed shortly afterward. With further increase in AOA, a LEV forms, and its corresponding low-pressure zone covers the suction side of the airfoil. At $\alpha_{eff} = 25^\circ$, the suction side is mostly covered by negative pressure. This negative pressure zone is close to the trailing edge, where the secondary LEV appears at the middle of the suction side. In Figures 9(g) and 9(h), notable low-pressure zones indicate shedding of core vortices. However, in Figure 9(i), we can not see any significant pressure gradient for formation of large aerodynamic loads.

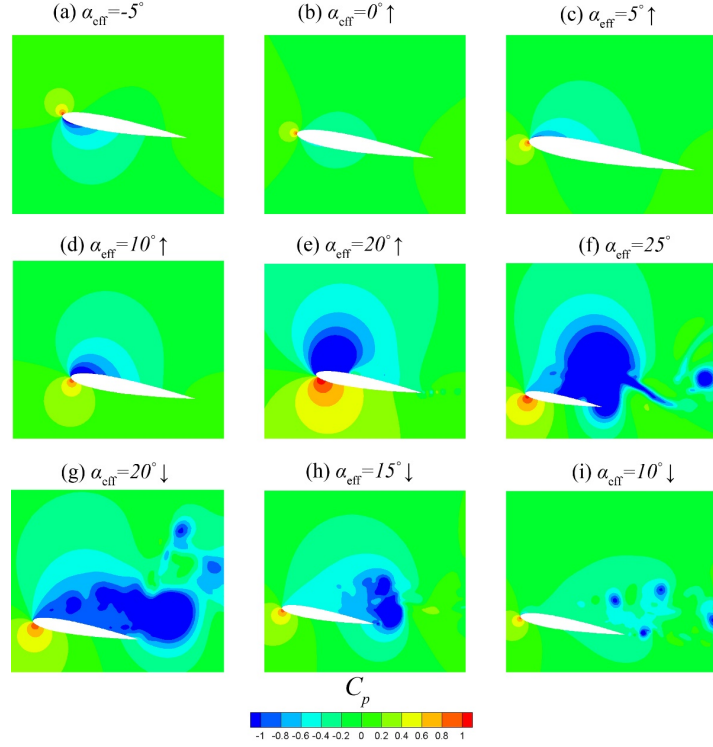


Figure 8: Pressure coefficient contours around a pure-heaving airfoil at $k = 0.1$.

294 4.2. Aerodynamics loads

In this section, the aerodynamic loads for this study are presented. Figure 10 illustrates the aerodynamic
 296 loads for different kinematic motions during one oscillation period at various reduced frequencies in x and y
 directions. Since the dynamic stall significantly impacts these forces, the aerodynamic loads in both directions
 298 are essential for controlling wind turbines.

As shown in Figure 10(a), the reduced frequency is $k = 0.05$, and the load variations in y direction change
 300 linearly in the pre-stall area. In this area, the AOA starts to increase to a moderate range, and the flow is
 mostly attached to the airfoil, and trailing edge separation occurs at moderate angles of attack. In the stall
 302 region, fluctuations appear due to the irregular flow pattern and presence of vortices. The slope and magnitude
 of force in y direction increases due to creation and growth of the LEV. On the other hand, there is a drop in
 304 the force in y direction due to the LEV pinch-off, and creation of the TEV at the leading edge of the airfoil.

At the beginning of the stall region, C_y for heaving motion has a slope change that indicates the LEV has
 306 higher strength than those in the pitching motion. The second peak in C_y also indicates a higher strength of
 the subsequent LEV. In the post-stall region, C_y for heaving and pitching is different in both magnitude and
 308 fluctuations. When the AOA decreases, the airfoil turns from post-stall into pre-stall, and flow attaches to the
 surface of the airfoil. In Figure 10(b), the reduced frequency is $k = 0.1$, and C_y increases linearly with increasing
 310 AOA in the pre-stall region for both heaving and pitching motion. The heaving motion in the pre-stall region
 results in lower C_y compared to that of the pure pitching motion. This is because the separation point on the
 312 suction side of the airfoil is advanced toward the trailing edge, and this causes less lift for pure heaving motion

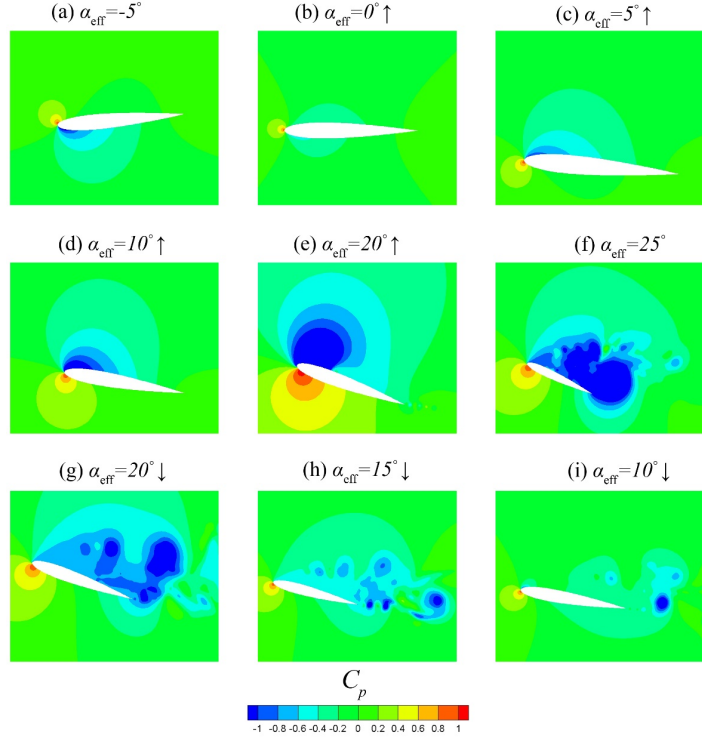


Figure 9: Pressure coefficient contours around a pure-pitching airfoil at $k = 0.1$.

in the pre-stall region. Figure 10(c) shows that the reduced frequency is $k = 0.2$, and the slope and magnitude of C_y for heaving motion increase early on in the stall region. In the first half of the post-stall region, the heaving motion produces a higher load, while in the second half of this region, C_y abruptly decreases, and the pitching motion shows a higher C_y . As the reduced frequency increases, the strength of vortices also increases. Hence, the aerodynamic loads in y direction have higher magnitudes with higher fluctuations. The heaving motion typically causes stronger core vortices in both the stall and post-stall regions. Furthermore, at lower reduced frequencies, the number of fluctuations in the aerodynamic loads increases, indicating the generation of more core vortices and shedding.

In Figure 10(d), the reduced frequency is $k = 0.05$, and in this case, C_x is relatively low in the pre-stall region. The aerodynamic load in x direction increases suddenly as the core vortices (LEV) appear in the oscillation period. Interestingly, there is a considerable difference between C_x for heaving and pitching motions. In heaving motion, C_x usually is lower than that of the pitching motion. In this case, the main fluctuations have low amplitudes, and when increasing the reduced frequency to $k = 0.1$, Figure 10(e), C_x increases notably for pitching motion. Furthermore, C_x for heaving motion becomes negative when the AOA is negative too, while for pitching motion, C_x is always positive.

When the reduced frequency is $k = 0.2$, Figure 10(f), for pitching motion, C_x still has abrupt changes with a comparable peak compared to the heaving motion. Generally, the pitching motion results in higher C_x for all ranges in reduced frequency. This means that most core vortices in the heaving motion contribute more in y direction. Additionally, as the reduced frequency increases, the magnitude and amplitude of the main

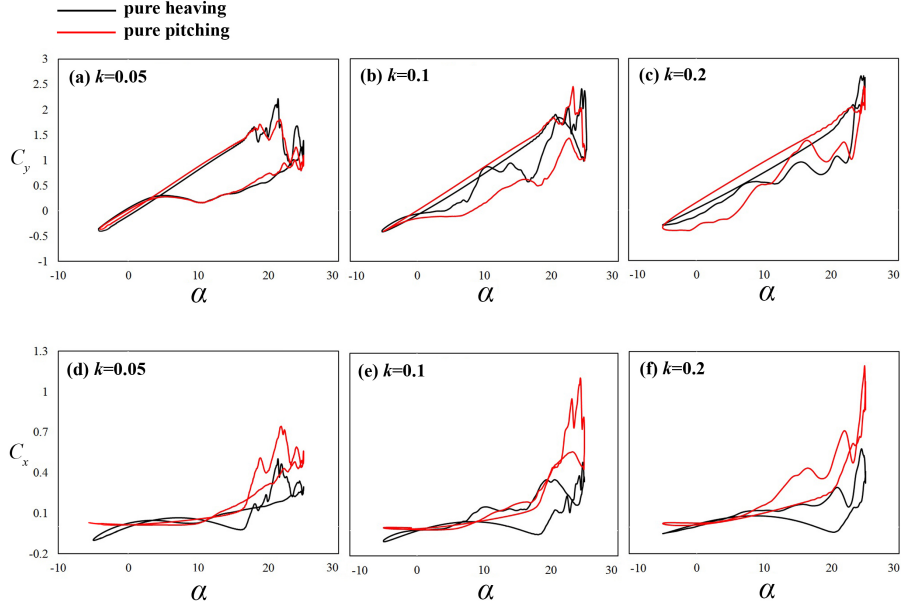


Figure 10: Aerodynamic loads in y direction, C_y , in one oscillation period for both pure-pitching and pure-heaving at different reduced frequencies: (a) $k = 0.05$; (b) $k = 0.1$; (c) $k = 0.2$.

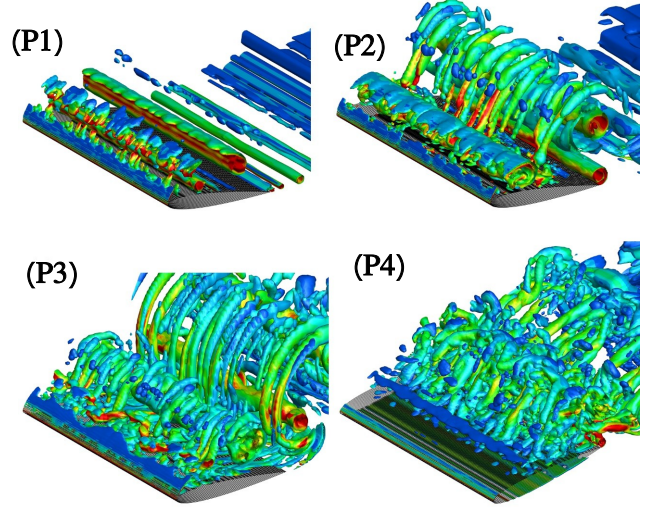
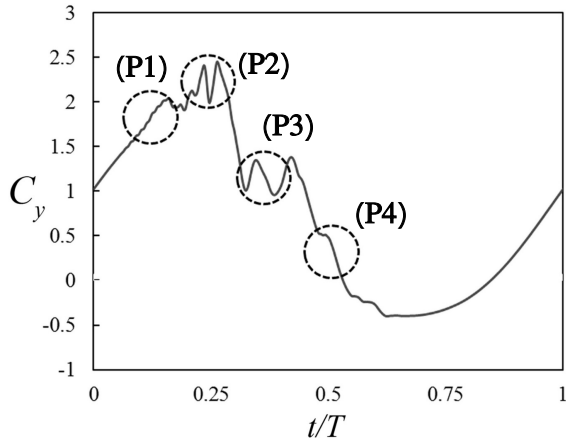
fluctuations increase. The rotation and transversal motion of the airfoil is responsible for changes in the incident AOA. In the pitching motion, the flow and incident velocity direction does not change, and just the rotation of the airfoil causes variations in the incident angle. Hence, the flow direction is the same as the free-stream direction, x direction. On the other hand, the transversal motion in heaving motion changes the velocity vectors and incident velocity direction. Therefore, the flow direction would be somewhere in between x and y directions. Thus, it is expected that the aerodynamic loads will contribute more in y direction. Additionally, in heaving motion, the incident velocity increases due to the airfoil's transversal motion, and it is expected that the shear stress at the leading edge to increase. This increment in the shear stress at the leading edge elevates turbulence kinetic energy inside the boundary layer. In this case, this shear stress injects more energy into the laminar separation bubbles, creating stronger LEVs.

4.3. Flow structure

In this section, the flow field around a moving airfoil is considered. Since flow structure analysis is relatively similar for all cases in different reduced frequencies, we decided to only consider the flow field at $k = 0.2$. Figures 11 is provided to assess the flow structure while the dynamic stall phenomenon happens. This figure also shows Q-criterion of iso-surface, coloured by vorticity magnitude.

In section "P1" in Figure 11, the airfoil has already passed the pre-stall region, and C_y starts to fluctuate instead of a linear increase as the AOA increases. These fluctuations indicate trailing edge separation and a premature LEV. Additionally, this kind of fluctuation might appear even at lower AOAs caused by von-Karman streets. In section "P2", C_y increases and reaches its peak, and a dynamic stall happens at this moment. As it is shown, the primary LEV envelopes the airfoil's suction side and is about to pinch-off due to rolling up of the TEV and its stimulation. Additionally, the secondary LEV is created and is fed by the severe shear layer

Pure pitching



Pure heaving

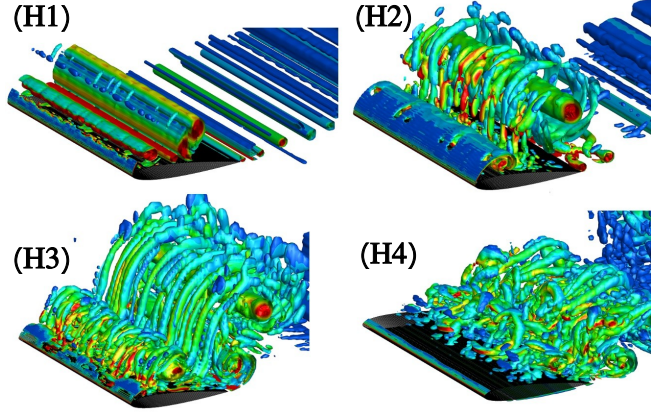
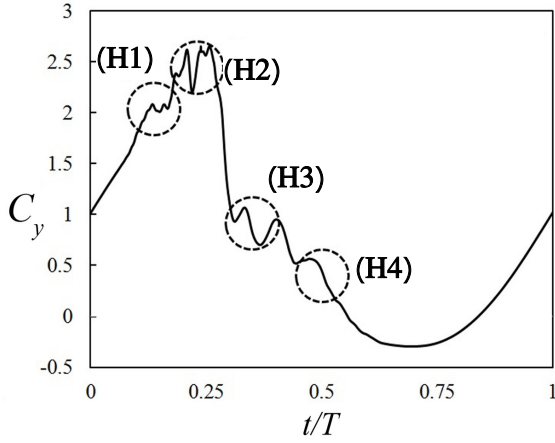


Figure 11: Instantaneous C_y and flow structures in one oscillation period for both pure-heaving and pitching motions at $k = 0.2$. The contours coloured by vorticity magnitude: a range from dark blue to red indicates those values from 0 to 400.

at the leading edge. In section “P3”, the AOA decreases, and TEV reaches its maximum circulation, while the primary LEV has already left the airfoil surface. Therefore, a sudden drop in C_y is expected while the secondary LEV is still developing to envelop the airfoil’s suction side. In section “P4”, the AOA is continuously decreasing, and C_y falls. At this instant, flow detachment has already started from the leading edge, and the flow is massively separated from the trailing edge section and sheds into the wake.

In the case of pure heaving motion, as the AOA increases from lower angles to moderate ones, C_y increases linearly in the pre-stall region. As shown in section “H1” in Figure 11, the slope and shape of C_y are changed, indicating LEV formation. As it is shown, the primary LEV is already formed and developed while moving toward the trailing edge. Additionally, the secondary LEV is being fed by the strong shear layer at the leading edge. In section “H2”, C_y reaches its peak, and it is expected that the circulation of LEV is near its maximum value. The circulation of the LEV is the maximum shortly after pinch-off, where the primary LEV covers most suction side area and imposes an intense low-pressure zone over the airfoil surface. Additionally, the secondary

LEV is still fed by the shear layer caused by the adverse pressure gradient at the leading edge. In section “H3”, the AOA decreases, and C_y falls since the pinch-off for the primary LEV has occurred. The TEV is promoted, and its circulation reaches its maximum value. It is expected that the secondary LEV will rise and makes another low-pressure zone over the suction side of the airfoil. Therefore, some fluctuations appear due to the secondary LEV in section “H3”. However, in section “H4”, the AOA is relatively low, and C_y decreases. At this moment, the flow is massively separated and sheds into the wake, while a strong shear layer at the leading edge vanishes due to the decreasing AOA. The shear layer’s disappearance leads to flow attachment near the leading edge and continues until the flow is mostly attached to the airfoil surface.

4.4. Turbulence

To examine the turbulence characteristics regarding dynamic stall, Figure 12 is provided to investigate the turbulence near the shear flow and the wake. The turbulence was measured for all cases for both heaving and pitching motions. Points A and B are locations in the computational domain, where data acquisition are made. Both points are located in the middle of the straight airfoil. Point A is located at $0.3c$ away from the leading edge, and its distance from the surface of the airfoil is $0.1c$. Point B is located behind the airfoil with a distance of $0.1c$ away from the trailing edge. It is worth mentioning that the location of these points remain unchanged in domain. This is because of limitations that exist in data acquisition from the moving meshes.

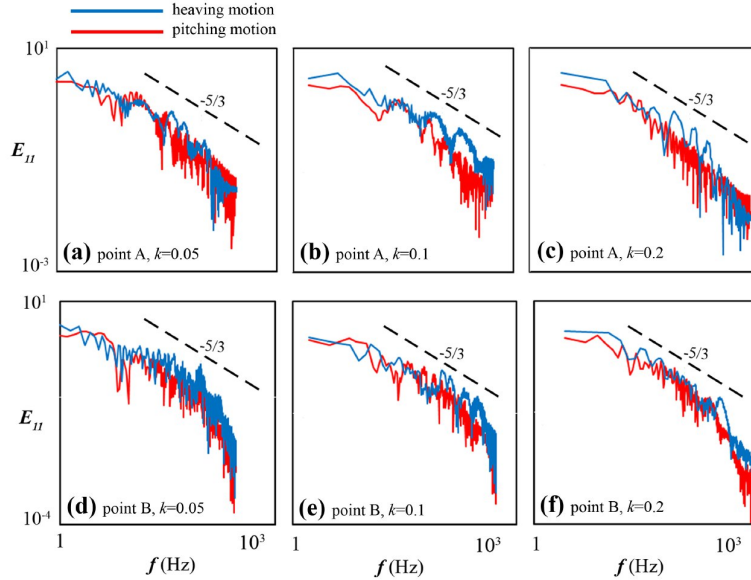


Figure 12: Stream-wise turbulence kinetic energy spectrum versus frequency for both heaving and pitching motions. The measurements were done in two distinct points in the 2D flow field domain in the middle of a straight airfoil.

380

Figure 12 shows that the stream-wise energy spectrum versus frequency was computed using a Fast-Fourier Transform (FFT). Figures 12(a), 12(b), and 12(c) show the turbulence kinetic energy for point A. At low frequencies, the turbulent kinetic energy near the shear layer for an airfoil with the heaving motion is mostly higher than that of the pitching motion. This fact indicates the existence of large-scale coherent structures, which have lower frequencies, near the shear layer or the wake region, and their energies are higher when the

airfoil has the heaving motion compared to the pitching motion. Therefore, the flow is more stable, and the boundary layer separation is delayed due to the higher kinetic energy in the boundary layer in reversal flow near the airfoil surface. In the inertial sub-range, the airfoil's kinetic energy with heaving motion is also higher than that of the pitching motion.

Figures 12(d), 12(e), and 12(f) show the turbulence kinetic energy extracted at point B. At lower frequencies, the large-scale coherent structures in the wake of the airfoil with heaving motion have more energy than the pitching motion. As mentioned, the heaving motion adds another velocity component in y direction, which affects the incident velocity and adds extra kinetic energy to the boundary layer. Although this pitching motion adds a non-uniform incident velocity to the kinematics, its effect on the flow is negligible compared to the one added by heaving motion. This is because the displacement of the airfoil for pitching motion is very less than that of the heaving one. Hence, the large-scale coherent structures for the airfoil with heaving motion are more energetic. Additionally, with increasing the reduced frequency, the frequency range for the energy spectrum also increases. The flow field contains more small-scale structures with high frequencies at a higher reduced frequency of the airfoil.

In summary, a airfoil with a heaving motion adds more kinetic energy to the boundary layer. Near the shear layer close to the leading edge, this extra energy causes the separation point to move toward the leading edge with some delay compared to that of the pitching motion. There are large-scale coherent structures in the wake of the airfoil, and the energetic structures have more energy for heaving motion than pitching. Therefore, as shown in Figure 10, in the pre-stall region, the heaving motion makes a lower lift force than the pitching motion because of the delay in transferring the separation point. However, in the stall region, the heaving motion has more energetic structures, and the lift coefficient is mostly higher near the stall region. Additionally, because of the delay in transferring the separation point, the drag force for the heaving motion usually is lower than that of the pitching motion.

5. Conclusions

In the present work, the flow field around a moving airfoil with different kinematics was numerically studied. This study looks at the dynamic stall of wind turbines from a different perspective. Since full-simulation of flow around a wind turbine is computationally expensive, we decided to investigate the dynamic stall features around a straight and finite airfoil. The CFD method was applied to simulate the flow structure in a 3D domain. To solve the Navier-Stokes equations, the DDES approach was employed as a hybrid model to solve the flow field in the massive flow separations and the wake behind the airfoil in unstable conditions. Inside the boundary layer, the URANS accompanied by SST $k - \omega$ turbulence model was employed, and the flow in the wake was solved using LES. The Reynolds number was set to $Re = 1.35 \times 10^5$, and the reduced frequency was between 0.05 and 0.2. The airfoil had pure-pitching and pure-heaving moving patterns with an equivalent AOA profile and the same operational conditions. Additionally, the pure-heaving can stabilize core vortices in the stall, leading to stronger LEVs and higher lift force compared to pure-pitching motion. Interestingly, the pitching motion induces a higher drag coefficient than pure-heaving motion, indicating the flow structure mechanism for these

two distinct motions is quite different. Therefore, in the design of large wind turbines where the dynamic stall is a significant problem, the airfoil's kinematics and aeroelasticity should be examined with pure-pitching and pure-heaving patterns to approximate aerodynamic load variations correctly.

6. Acknowledgment

This work was supported by Brain Pool Program through the National Research Foundation of Korea (NRF) funded by the Ministry of Science and ICT (NRF- 2020A1D3A2A01104062). This work was also supported by the National Research Foundation of Korea (NRF) grant, which is funded by the Korean government (MSIT) (No. 2020R1A5A8018822).

References

- [1] J. Liiva, Unsteady aerodynamic and stall effects on helicopter rotor blade airfoil sections., *Journal of Aircraft* 6 (1) (1969) 46–51.
- [2] W. J. McCroskey, Unsteady airfoils, *Annual review of fluid mechanics* 14 (1) (1982) 285–311.
- [3] W. J. McCroskey, The phenomenon of dynamic stall., Tech. rep., National Aeronautics and Space Administration Moffett Field Ca Ames Research ... (1981).
- [4] H. F. Müller-Vahl, C. Strangfeld, C. N. Nayeri, C. O. Paschereit, D. Greenblatt, Control of thick airfoil, deep dynamic stall using steady blowing, *AIAA journal* 53 (2) (2015) 277–295.
- [5] S. Gupta, J. G. Leishman, Dynamic stall modelling of the s809 aerofoil and comparison with experiments, *Wind Energy: An International Journal for Progress and Applications in Wind Power Conversion Technology* 9 (6) (2006) 521–547.
- [6] C. Butterfield, D. Simms, G. Scott, A. Hansen, Dynamic stall on wind turbine blades, Tech. rep., National Renewable Energy Lab., Golden, CO (United States) (1991).
- [7] C. Zhu, J. Chen, J. Wu, T. Wang, Dynamic stall control of the wind turbine airfoil via single-row and double-row passive vortex generators, *Energy* 189 (2019) 116272.
- [8] A. Rezaeiha, H. Montazeri, B. Blocken, Cfd analysis of dynamic stall on vertical axis wind turbines using scale-adaptive simulation (sas): Comparison against urans and hybrid rans/les, *Energy Conversion and Management* 196 (2019) 1282–1298.
- [9] A. Choudhry, M. Arjomandi, R. Kelso, Methods to control dynamic stall for wind turbine applications, *Renewable energy* 86 (2016) 26–37.
- [10] Y. Kim, Z.-T. Xie, Modelling the effect of freestream turbulence on dynamic stall of wind turbine blades, *Computers & Fluids* 129 (2016) 53–66.

- [11] W. J. McCroskey, K. McAlister, L. Carr, S. Pucci, O. Lambert, R. Indergrand, Dynamic stall on advanced airfoil sections, *Journal of the American Helicopter Society* 26 (3) (1981) 40–50.
- [12] A. Buchner, M. W. Lohry, L. Martinelli, J. Soria, A. J. Smits, Dynamic stall in vertical axis wind turbines: comparing experiments and computations, *Journal of Wind Engineering and Industrial Aerodynamics* 146 (2015) 163–171.
- [13] K. Gharali, D. A. Johnson, Effects of nonuniform incident velocity on a dynamic wind turbine airfoil, *Wind Energy* 18 (2) (2015) 237–251.
- [14] H. R. Karbasian, J. Esfahani, E. Barati, Effect of acceleration on dynamic stall of airfoil in unsteady operating conditions, *Wind Energy* 19 (1) (2016) 17–33.
- [15] J. Zhong, J. Li, P. Guo, Y. Wang, Dynamic stall control on a vertical axis wind turbine aerofoil using leading-edge rod, *Energy* 174 (2019) 246–260.
- [16] H. R. Karbasian, S. Moshizi, M. J. Maghrebi, Dynamic stall analysis of s809 pitching airfoil in unsteady free stream velocity, *Journal of Mechanics* 32 (2) (2016) 227–235.
- [17] C. S. Ferreira, H. Bijl, G. Van Bussel, G. Van Kuik, Simulating dynamic stall in a 2d vawt: modeling strategy, verification and validation with particle image velocimetry data, in: *Journal of physics: conference series*, Vol. 75, IOP Publishing, 2007, p. 012023.
- [18] K. Almohammadi, D. Ingham, L. Ma, M. Pourkashanian, Modeling dynamic stall of a straight blade vertical axis wind turbine, *Journal of Fluids and Structures* 57 (2015) 144–158.
- [19] J. Yen, N. A. Ahmed, Enhancing vertical axis wind turbine by dynamic stall control using synthetic jets, *Journal of Wind Engineering and Industrial Aerodynamics* 114 (2013) 12–17.
- [20] X. Liu, C. Lu, S. Liang, A. Godbole, Y. Chen, Vibration-induced aerodynamic loads on large horizontal axis wind turbine blades, *Applied Energy* 185 (2017) 1109–1119.
- [21] W. Mo, D. Li, X. Wang, C. Zhong, Aeroelastic coupling analysis of the flexible blade of a wind turbine, *Energy* 89 (2015) 1001–1009.
- [22] H. R. Karbasian, K. C. Kim, Numerical investigations on flow structure and behavior of vortices in the dynamic stall of an oscillating pitching hydrofoil, *Ocean Engineering* 127 (2016) 200–211.
- [23] J. Panda, K. B. Zaman, Experimental investigation of the flow field of an oscillating airfoil and estimation of lift from wake surveys, *Journal of Fluid Mechanics* 265 (1994) 65–95.
- [24] M. M. Amiri, M. Shadman, S. F. Estefen, Urans simulations of a horizontal axis wind turbine under stall condition using reynolds stress turbulence models, *Energy* 213 (2020) 118766.

- [25] M. Boudreau, K. Gunther, G. Dumas, Investigation of the energy-extraction regime of a novel semi-passive flapping-foil turbine concept with a prescribed heave motion and a passive pitch motion, *Journal of Fluids and Structures* 84 (2019) 368–390.
- [26] H. R. Karbasian, J. Esfahani, Enhancement of propulsive performance of flapping foil by fish-like motion pattern, *Computers & Fluids* 156 (2017) 305–316.
- [27] D. Moreira, N. Mathias, T. Morais, Dual flapping foil system for propulsion and harnessing wave energy: A 2d parametric study for unaligned foil configurations, *Ocean Engineering* 215 (2020) 107875.
- [28] H. Karbasian, J. A. Esfahani, E. Barati, The power extraction by flapping foil hydrokinetic turbine in swing arm mode, *Renewable Energy* 88 (2016) 130–142.
- [29] Y. Wang, X. Sun, D. Huang, Z. Zheng, Numerical investigation on energy extraction of flapping hydrofoils with different series foil shapes, *Energy* 112 (2016) 1153–1168.
- [30] M. M. Koochesfahani, Vortical patterns in the wake of an oscillating airfoil, *AIAA journal* 27 (9) (1989) 1200–1205.
- [31] K. Jones, C. Dohring, M. Platzer, Experimental and computational investigation of the knoller-betz effect, *AIAA journal* 36 (7) (1998) 1240–1246.
- [32] J. Young, J. C. Lai, Oscillation frequency and amplitude effects on the wake of a plunging airfoil, *AIAA journal* 42 (10) (2004) 2042–2052.
- [33] J. Young, J. C. Lai, Mechanisms influencing the efficiency of oscillating airfoil propulsion, *AIAA journal* 45 (7) (2007) 1695–1702.
- [34] A. R. Davari, Wake structure and similar behavior of wake profiles downstream of a plunging airfoil, *Chinese Journal of Aeronautics* 30 (4) (2017) 1281–1293.
- [35] G. Chang, H. R. Karbasian, S. Zhang, Y. Yan, B. Chen, K. C. Kim, The influence of kinematics of blades on the flow structure in deep dynamic stall, *Journal of Mechanical Science and Technology* 34 (7) (2020) 2855–2868.
- [36] W. Medjroubi, B. Stoevesandt, B. Carmo, J. Peinke, High-order numerical simulations of the flow around a heaving airfoil, *Computers & Fluids* 51 (1) (2011) 68–84.
- [37] B. Hand, G. Kelly, A. Cashman, Numerical simulation of a vertical axis wind turbine airfoil experiencing dynamic stall at high reynolds numbers, *Computers & Fluids* 149 (2017) 12–30.
- [38] L. Zhenyao, F. Lihao, H. R. Karbasian, W. Jinjun, K. C. Kim, Experimental and numerical investigation of three-dimensional vortex structures of a pitching airfoil at a transitional reynolds number, *Chinese Journal of Aeronautics* 32 (10) (2019) 2254–2266.
- [39] P. Lissaman, Low-reynolds-number airfoils, *Annual review of fluid mechanics* 15 (1) (1983) 223–239.

- ⁵¹⁴ [40] H. Hu, Z. Yang, An experimental study of the laminar flow separation on a low-reynolds-number airfoil, Journal of Fluids Engineering 130 (5) (2008).
- ⁵¹⁶ [41] T. Lee, P. Gerontakos, Investigation of flow over an oscillating airfoil, Journal of Fluid Mechanics 512 (2004) 313.